Inorganic Chemistry

Article

pubs.acs.org/IC

New Twists on the Perovskite Theme: Crystal Structures of the Elusive Phases R and S of $NaNbO_3$

Martin D. Peel,[†] Stephen P. Thompson,[‡] Aziz Daoud-Aladine,[§] Sharon E. Ashbrook,[†] and Philip Lightfoot*[,†]

[†]School of Chemistry and EaStCHEM, University of St. Andrews, St. Andrews, KY16 9ST, United Kingdom

[‡]Diamond Light Source Limited, Harwell Science and Innovation Campus, Didcot, OX11 0DE, United Kingdom

[§]ISIS Facility, Rutherford Appleton Laboratory, Chilton, Didcot, OX11 0QX, United Kingdom

Supporting Information

ABSTRACT: The crystal structure of $NaNbO_3$ has been studied in detail in the temperature regime 360 < T < 520 °C using a combination of high-resolution neutron and synchrotron X-ray powder diffraction, supported by first-principles calculations. A systematic symmetry-mode analysis is used to determine the presence of the key active distortion modes that, in turn, provides a small and an unambiguous set of trial structural models. A unique model for Phase S (480 < T < 510 °C) is elucidated, having a 2 × 2 × 4 superlattice of the aristotype perovskite structure, space group *Pmmn*. This unusual and unique structure features a novel example of a *compound* octahedral tilt system in a perovskite. Two possible structural models for Phase R (370 < T < 470 °C) are determined, each having a 2 × 2 × 6 superlattice and differing only in the nature of the complex tilt system along the 'long' axis. It is impossible to identify a definitive model from the present study, although reasons for preferring one over the other are discussed. Some of the possible pitfalls in determining such complex, pseudosymmetric crystal structures from powder diffraction data are also highlighted.

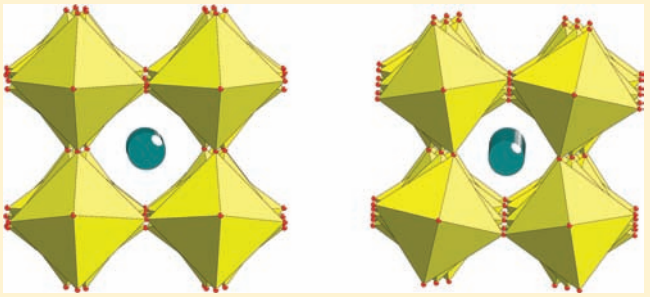

INTRODUCTION

Sodium niobate, $NaNbO_3$, has been described as 'the most complex ferroelectric perovskite known'[1] and the subject of a large number of crystallographic studies during the past 50 years or more. Aside from its intrinsic fundamental interest, $NaNbO_3$ has recently enjoyed renewed study as an important funtional material, since the discovery of very promising piezoelectric properties in some of its solid solutions.[2] Much of the key early crystallographic work was carried out by Megaw and co-workers.[3−7] Megaw summarized the state of the art in the 1974 paper 'The seven phases of sodium niobate'.[8] In fact, the 'seven phases' refers to only those which arise from a sequential series of phase transitions versus temperature. At that time there was an additional, ferroelectric phase known ('Phase Q'), which could be induced by an electric field at room temperature but was also visible as a coexisting phase during some heating regimes.[3] More recent work has clarified the nature of this phase somewhat,[9,10] and there have also been recent reports of at least two further room-temperature polymorphs obtained by soft-chemical routes.[11,12] The original sequence of seven phases was designated by the labels N (stable below −100 °C), P (−100 to 360 °C), R (360−480 °C), S (480−520 °C), T1 (520−575 °C), T2 (575−640 °C), and U (>640 °C). The crystal structures of N, P, T1, T2, and U have been well established,[6,13−16] with phase P being of particular structural interest as it has a relatively complex 'octahedral tilt' system, which does not fit into the standard Glazer scheme.[17,18] This tilt system results in a quadrupling of the aristotype cubic perovskite unit cell dimension, a_p, along one axis, caused by a complex tilt mode (in Glazer notation designated $a^-a^-b^+/a^-a^-b^-/a^-a^-b^+$). Careful measurements of lattice parameter metrics and key superlattice reflections from the early single-crystal work suggested that phases R and S also have more complex tilt systems, and tentative structural models were proposed[4,6] but without full structural refinement.

Since then there have been several attempts to solve the crystal structures of phases R and S,[16,19−22] most often using neutron powder diffraction (NPD) methods, but there is still disagreement in the recent literature on their precise nature. It is evident that $NaNbO_3$ is susceptible to several competing structural instabilities, giving rise to an array of phases with very similar free energies.[23,24] The difficulties inherent in the precise structural characterization of this system arise from the structural similarities between these competing phases and the consequent ambiguities and pseudosymmetries present in their diffraction patterns. One way to ameliorate these ambiguities is to use principles based on the likely distortion

Received: March 30, 2012
Published: June 5, 2012

   dx.doi.org/10.1021/ic3006585 | *Inorg. Chem.* 2012, 51, 6876−6889

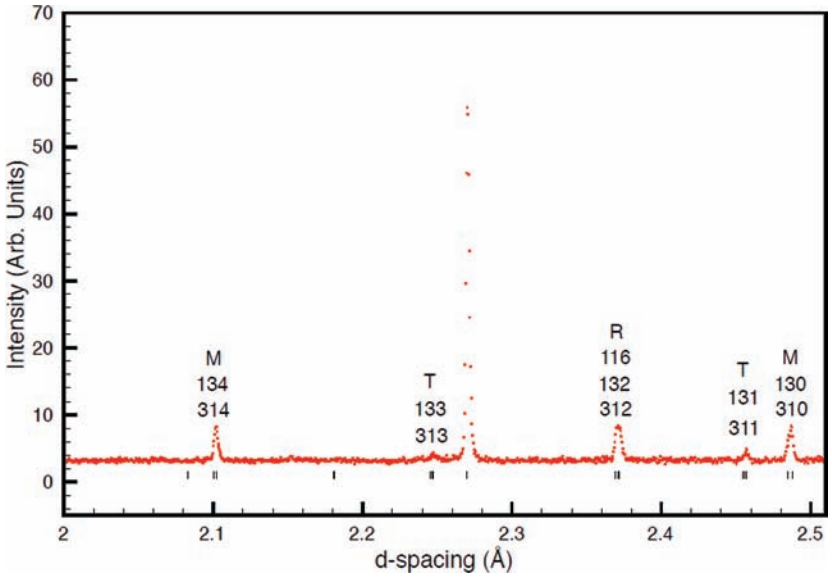

Figure 1. Portion of the raw NPD data for phase S at 500 °C showing superlattice peaks at the M, R, and T points (indices refer to the $2a_p \times 2a_p \times 4a_p$ *C*-centered supercell).

modes of the aristotype perovskite to guide the choice of plausible starting models for structural analysis. Such methods have, of course, been exploited widely in simpler perovskite systems which correspond to the original Glazer systems.[18,25] Typically, the key drivers for the distortions in simple perovskites are octahedral tilt modes (generally dictated by cation size effects), ferroelectric cation displacements, and other displacement modes such as Jahn–Teller distortions. These modes are now amenable to relatively straightforward and systematic analysis with the advent of user-friendly software which analyze distortions away from high-symmetry aristotype structures via decomposition into symmetry modes derived from irreducible representations (*irreps*).[26,27] In the language of physics these symmetry modes represent 'frozen' phonon modes at particular points in the Brillouin zone. For example, the mode giving rise to the simple Glazer tilt system $a^0a^0c^+$ (as seen in $NaNbO_3$ phase T2) is characterized by the *irrep* M_3^+, which condenses at the M point (k = (1/2, 1/2, 0)) in the Brillouin zone of the aristotype cubic perovskite.

In this paper we address the completion of the $NaNbO_3$ phase diagram by carrying out a detailed and systematic analysis of the possible structures for phases R and S through exploitation of the complementarity of neutron and X-ray powder diffraction, coupled with symmetry mode analysis using the ISODISTORT software. In deriving our models, no reference was made to previous suggested models.

EXPERIMENTAL SECTION

A sample of $NaNbO_3$ was purchased from Sigma-Aldrich (99.9%) and used without further purification. Phase purity was checked carefully using powder X-ray diffraction on a Stoe STADI-P X-ray diffractometer using Cu $K\alpha_1$ (λ = 1.54056 Å) radiation. In particular, a careful check was made for the absence of the polar "$P2_1ma$" polymorph, which often coexists, depending on sample preparation method.[9] The presence of only the antiferroelectric phase P[14] was confirmed.

Powder Diffraction. Time-of-flight neutron powder diffraction (NPD) experiments were conducted using the high-resolution powder diffractometer (HRPD) at the ISIS neutron spallation source, Rutherford-Appleton Laboratories. The polycrystalline sample (~4 g) was mounted in a cylindrical vanadium can within a standard furnace. Data were collected at temperatures of 20, 200, 320, 340, and 360 °C and then at 10 °C intervals from 370 to 530 °C, inclusive. Each scan was counted for 20 μAhr (ca. 30 min). Synchrotron X-ray powder diffraction (SXPD) data were collected using the multianalyzing crystal (MAC) system on beamline I-11[28] at Diamond at a wavelength of 0.82503 Å. The sample was mounted in a quartz capillary (0.5 mm diameter), which was heated using a hot-air blower (10 °C min^{-1}) over the temperature range from 100 to 660 °C at 20 °C intervals. Each scan was recorded for 15 min, with a temperature equilibration of 10 min allowed between scans.

All diffraction data were analyzed by Rietveld refinement using the General Structure Analysis System (GSAS) software package.[29] Parameters refined included background coefficients, lattice parameters, profile coefficients, grouped isotropic atomic displacement parameters, and atomic positional coordinates. Further details of specific refinement strategies, including constraints used, are given in the appropriate section and also in the Supporting Information. Symmetry mode analysis was carried out using the ISODISTORT software.[27]

Calculations. First-principles calculations were carried out using the CASTEP density functional theory (DFT) code,[30] a planewave pseudopotential method using the gauge-including projector-augmented wave (GIPAW) formalism.[31] The Perdew–Burke–Ernzerhof (PBE) parametrization of the generalized gradient approximation (GGA) was employed, and core–valence electron interactions were described using ultrasoft pseudopotentials.[32] A cutoff energy of 60 Ry was used, with a k-point spacing of 0.04 Å^{-1}. Calculations were carried out at the University of St. Andrews using CASTEP version 5.5.2 on a 198-node (2376 core) Intel Westmere cluster with 2 GB memory per core and QDR Infiniband interconnect.

RESULTS AND DISCUSSION

Preliminary Data Analysis. Rietveld refinement of both NPD and SXPD data at room temperature revealed an excellent fit to the anticipated phase P model in space group *Pbcm*. This phase continued to exist uniquely until 360 °C, whereupon the appearance of an additional phase (R) was revealed, in agreement with earlier work. Unfortunately the SXPD data could not be used satisfactorily in the analysis of phase S, since coexistence of either phases P and S or phases S and R was observed in each data set collected throughout this temperature region (due to the larger temperature step size). At this point attention was therefore focused on analysis of the

dx.doi.org/10.1021/ic3006585 | *Inorg. Chem.* 2012, 51, 6876–6889

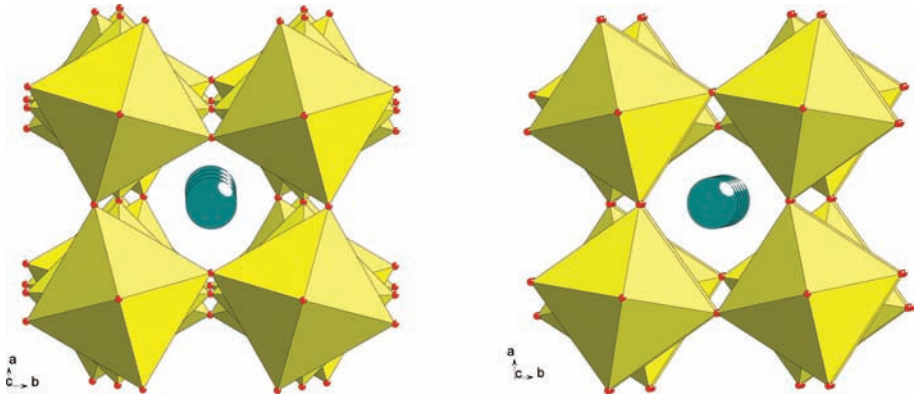

Figure 2. Tilt modes of the two possible T_4 *irreps* that can operate in the $2a_p \times 2a_p \times 4a_p$ supercell: (a) A0C0 and (b) AACC.

NPD data only, although we shall return to the X-ray data in due course (for phase R). Examination of the raw NPD data at 370 °C suggested several key superlattice peaks that were characteristic of phase R, and these disappeared completely between 470 and 480 °C. The 500 °C data set was therefore assumed to represent pure phase S.

Phase S at 500 °C. A portion of the raw NPD data is shown in Figure 1. This plot illustrates several important features. Most significantly, several key superlattice reflections can be seen, which can be used to pinpoint the multiplicity and dimensions of the supercell. The peak at $d \approx 2.27$ Å is the $(111)_p$ subcell peak; the peaks at $d \approx 2.49$, 2.37, and 2.10 Å are indexable only by applying a $\sqrt{2}a_p \times \sqrt{2}a_p$ or a $2a_p \times 2a_p$ cell expansion in the *ab* plane; the peaks at $d \approx 2.45$ and 2.24 Å are only indexable by applying an additional $4a_p$ expansion along the *c* axis. In fact, as will be shown below, the minimum cell metrics compatible with the observed peaks in this region are $2a_p \times 2a_p \times 4a_p$, with a *C*-centered orthorhombic symmetry. The peaks shown in Figure 1 therefore refer to indexing in the $2a_p \times 2a_p \times 4a_p$ *C*-centered orthorhombic supercell. The capital letters refer to corresponding points in the parent cubic Brillouin zone, described below.

The simplest and most systematic way of deriving possible starting models for structure elucidation is to use distortion mode analysis. The ISODISTORT software[27] allows derivation of all possible distorted models based on a parent structure, compatible with a given unit cell size and symmetry. In the present case, two initial searches were conducted: category (i) all supercells derived from the aristotype cubic perovskite ($a_p \approx$ 3.9 Å) having a $\sqrt{2}a_p \times \sqrt{2}a_p \times 4a_p$ metric and primitive tetragonal symmetry, point group 4/*mmm*, and category (ii) all supercells having a $2a_p \times 2a_p \times 4a_p$ metric and with *C*-centered orthorhombic symmetry, point group *mmm* (note that this naturally includes primitive orthorhombic supercells with a $\sqrt{2}a_p \times \sqrt{2}a_p \times 4a_p$ metric and *mmm* symmetry, since these lattices are equivalent prior to any further distortion). Here we are making the assumption that the observed phases are centrosymmetric (it would be highly unusual for the centrosymmetric phase P to transform to a noncentrosymmetric phase at higher temperature, and our successful analysis ultimately supports our assumption). In addition, although point group 4/*m* is a possibility at this stage, we soon show that tetragonal metrics are not compatible with the observed data. ISODISTORT lists 60 primitive tetragonal supercells in category (i) and 40 C-centered cells and 40 primitive cells in category (ii).

We emphasize that this analysis represents an *exhaustive* search of *all* possible ways to distort the aristotype cubic perovskite structure within the symmetry constrains imposed (later we go on to show that even these options are insufficient and a further lowering of symmetry to consider $2a_p \times 2a_p \times 4a_p$ primitive orthorhombic (*mmm* point group) unit cells is required).

The large number of options in categories (i) and (ii) arises in part due to various different origin choices in lowering the symmetry of the cubic aristotype. In order to simplify the options it is reasonable to make one further simple assumption which is ubiquitous in the analysis of distorted perovskites: the *dominant* distortion modes are those which derive from the tilting of rigid BO_6 octahedra. The validity of this assumption can be seen by analyzing the distortions observed in the previously well-characterized $NaNbO_3$ polymorphs. The relevant distortion modes relate to condensation at three specific points or lines in the Brillouin zone, the M, R and T points, and they are labeled M_3^+, R_4^+, and T_4, for the specific case of octahedral tilt modes only (note that the T point is specifically the $k = (1/2, 1/2, 1/4)$ point on the generic T line $((1/2, 1/2, \gamma)$, and the M and R points have fixed values, $k = (1/2, 1/2, 0)$ and $(1/2, 1/2, 1/2)$, respectively).

Each of these distortion modes gives rise to particular 'systematic presences' in the diffraction pattern. For the M_3^+ mode the observed Miller indices (referred to the *C*-centered supercell) have the form (odd, odd, 4*n*), for R_4^+ (odd, odd, 2*n*), and for T_4 (odd, odd, odd). Note at this stage we do not discriminate between *a* and *b* axes and correspondingly between *h, k* indices. There is also no implication of which axis the M_3^+ or R_4^+ mode refers to: they represent simply 'in-phase' or 'out-of-phase' tilts relative to a principal axis of the cubic aristotype ('+' or '−' tilts, respectively, in Glazer notation). Glazer notation is applicable to only $2 \times 2 \times 2$ supercells of the basic perosvkite aristotype. Therefore, we use a new notation that describes the tilts around the *c* axis in terms of clockwise (C), anticlockwise (A), or zero (0) tilts of adjacent octahedra (capital letters are used to avoid confusion with the Glazer notation). In this notation, the magnitudes of the C and A tilts are symmetry constrained to be equal. There are two different tilt modes of T_4 symmetry allowed in this supercell (Figure 2), which we designate as A0C0 and AACC.

Looking again at the observed superlattice reflections in Figure 1, the observed "(130/310)" and "(134/314)" peaks necessitate the presence of the M_3^+ mode, the "(132/312/116)" require R_4^+, and the "(131/311)" and "(133/313)" require the T_4 mode. Although there are in some supercells

dx.doi.org/10.1021/ic3006585 | *Inorg. Chem.* 2012, 51, 6876−6889

other contributions to the diffraction pattern of M, R, or T symmetry, these are typically modes which *distort* the octahedra or displace cations; it is reasonable to assume that at least the strongly observed M and R features are predominantly due to the M_3^+ and R_4^+ tilt modes: the much smaller observed intensities in the T mode peaks could, in principle, also arise from atomic (cation or anion) displacements or octahedral distortions, and this possibility is allowed for in the following analysis.

The next step involves a systematic search through each of the possibilities listed in category (i) and each of the *C*-centered options in category (ii) above to search for the *simultaneous* presence of the M_3^+ and R_4^+ modes. Of the available options, there are only four tetragonal models and three *C*-centered orthorhombic models fulfilling the requirement of simultaneous M_3^+ and R_4^+ modes. A systematic and self-consistent approach was used in testing each of the trial models. Each refinement used only the highest resolution detector bank with a *d*-spacing range ≈ 0.7 Å $< d <$ 2.5 Å. Four background coefficients, three peak-shape parameters (σ-1, σ-2, and γ-1), and scale factor were refined together with the necessary lattice parameters and individual isotropic atomic displacement parameters.

The *P*4/*mbm* model (S-T1) was tested first: this model allows the anticipated T_4 mode in addition to the M_3^+ and R_4^+ modes, whereas the other tetragonal models do not. Final refinement details are given in Table 1. The resulting fit of the *d* = 2.0−2.5 Å region appears very good at first sight (Figure S1, Supporting Information); in particular the three different types of superlattice peaks, at the R, M and T points, appear well modeled. Note that in the tetragonal system there is no option of octahedral tilting relative to the *a* or *b* axes. In other words, all three octahedral tilt modes are simultaneously present around the *c* axis! The model also permits displacements of both Na and Nb cations along *c*. Although this model appears superficially quite close to a valid structural model for phase S, closer inspection of the Rietveld fit over the full data range reveals problems. For example, the fit to the peak(s) at ∼1.95 Å (equivalent to the $(200)_p$ reflection in the parent cubic unit cell) is not adequate (Figure S2, Supporting Information), and the split R and M point superstructure peaks near *d* = 2.37 and 2.49 Å are clearly not accounted for. These inadequacies suggest a further lowering of symmetry to either the $\sqrt{2}a_p \times \sqrt{2}a_p \times 4a_p$ primitive orthorhombic cell or the $2a_p \times 2a_p \times 4a_p$ *C*-centered orthorhombic supercell. These two options can be distinguished by observing the relative 'splittings' (or 'broadenings') of the pseudocubic $(111)_p$ and $(200)_p$ peaks near *d* = 2.27 and 1.95 Å, respectively. The $(111)_p$ is split in the *P* cell but remains single in the *C* cell, whereas the (200) peak is allowed to split in both. It can be seen that the $(111)_p$ is sharp, and any attempts to lower the symmetry to a *P*-orthorhombic cell of metrics $\sqrt{2}a_p \times \sqrt{2}a_p \times 4a_p$ leads to a poorer fit due to the necessary splitting of this peak. Primitive orthorhombic cells of metric $\sqrt{2}a_p \times \sqrt{2}a_p \times 4a_p$ can therefore be ruled out.

Hence, the three possible *C*-centered orthorhombic cells were tested. Summaries of these refinements are given in Table 1. Of the three options, only the *Cmmm* model (S-C1) allows the T_4 octahedral tilt mode in addition to the M_3^+ and R_4^+ modes (the model can be considered as derived from the *P*4$_2$/*mbm* model, with the additional 'orthorhombic distortion' permitted). The *Cmcm* (S-C2) and *Cccm* (S-C3) models both allow other T-point modes, but these involve octahedral distortions or cation shifts. Although they provide some intensity for the T-mode peaks in Figure 1, the fits are significantly poorer than that for the S-C1 model. It can therefore be concluded that the S-C1 model, with three different tilt modes present *simultaneously* along the *c* axis (see Figure S3, Supporting Information), provides the optimal model so far. However, there are still inadequacies in the fit (Figure 3), such that we must also consider options that allow the R_4^+, M_3^+ (and T_4) tilt modes to be present along 2 or 3 different axes. This necessitates lowering of symmetry to the $2a_p \times 2a_p \times 4a_p$ primitive orthorhombic (*mmm* point group) options mentioned previously. There are 272 of these according to ISODISTORT! A systematic search through all of these possibilities looking for the simultaneous presence of R_4^+ and M_3^+ tilt modes *around two different axes* (plus optional T modes) revealed 15 options, listed in Table 2. In addition, there are several further two tilt-axis systems with both R_4^+ and M_3^+ modes relative to *the same axis* (*a* or *b*); unless these have the T_4 tilt in addition to these *compound a* or *b* axis tilts they need not be pursued further. There are two such options (S-P1 and S-P8) in Table 2. This appears to leave a bewildering array of possible models. However, a further subtlety can be exploited to identify a *unique* solution: examining closely the fit of the S-C1 model to the M-point peak near *d* = 2.49 Å (Figure 3), it can be seen that the calculated peak is a closely spaced symmetrical doublet. However, the observed peak clearly has an asymmetric character and/or a smaller splitting, and the resultant fit is poor. Assuming the peak arises predominantly from the M_3^+ tilt mode rather than other *distortive* M modes, this peak shape necessitates either the *simultaneous* presence of two or more M_3^+ modes or at least a lowering of symmetry to a situation where a single M_3^+ tilt corresponds to a different principal axis to the other tilt modes (i.e., it is not compatible with a tilt around the 'medium' axis). Inspection of Table 2 reveals there are only three options satisfying the requirement of multiple M_3^+ modes: S-P7, S-P12, and S-P16. Moreover, two of these, models S-P7 and S-P16, do not allow the additional T_4 tilt mode. Although there are other modes which might contribute to the T-line peaks, these can be ruled out on chemical grounds using ISODISTORT: any significant contribution to the observed T-line peaks shown in Figure 1

Table 1. Trial Models for Phase S at 500 °C in the Tetragonal, C-Centred, and Primitive Orthorhombic Models Discussed in the Text[a]

model	space group	N_{xyz}	N_{ref}	R_4^+ M_3^+ T_4	χ^2	R_{wp}
S-T1	*P*4/*mbm*	9	9	*m m m*	3.10	0.063
S-C1	*Cmmm*	15	15	*m m m*	2.28	0.054
S-C2	*Cmcm*	16	16	*m m -*	2.73	0.059
S-C3	*Cccm*	11	11	*m m -*	2.70	0.059
S-P12	*Pmmn*	33	4	*m l m*	1.92	0.050
S-P12a	*Pmmn*	33	33	*m l m*	1.80	0.048
S-P17	*Pnma*	31	31	*m l s*	1.85	0.049

[a] N_{xyz} is the number of allowed variable atomic coordinates; N_{ref} is the number actually refined, taking into account constraints imposed by the tilt modes. Individual isotropic atomic displacement parameters were used for the T and C models; these were grouped by element type for the P models. The same set of profile parameters was refined in each case. Symbols *s*, *m*, *l* in the fifth column represent the relative magnitudes ('small', 'medium', large') of the subcell axes, a_p, along which the three principal tilt modes act: the unique requirement of "*m l m*" for R_4^+, M_3^+, T_4, respectively, makes the final choice of model S-P12 unambiguous. The refined unit cell parameters for model S-P12a are *a* = 7.85684(4) Å, *b* = 7.86748(7) Å, *c* = 15.72795(13) Å.

dx.doi.org/10.1021/ic3006585 | *Inorg. Chem.* 2012, 51, 6876−6889

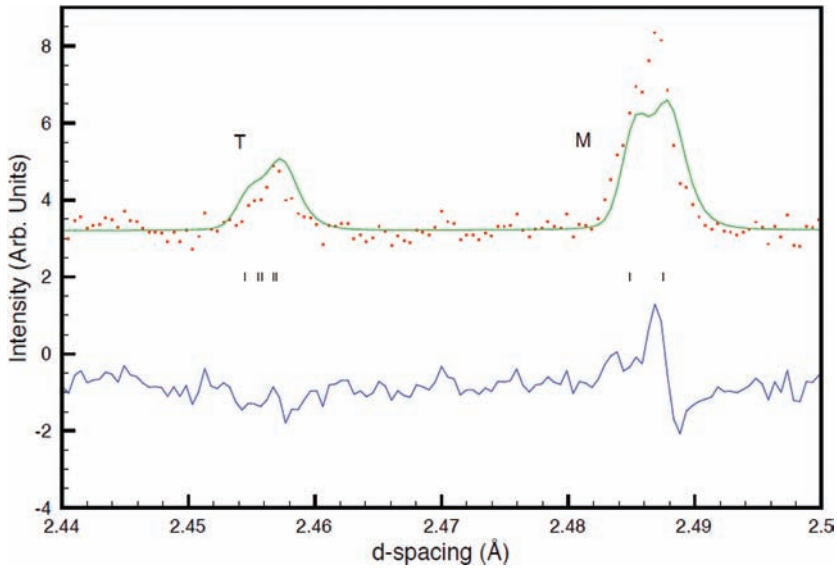

Figure 3. Portion of the Rietveld fit (NPD) to the S-C1 model at 500 °C. Note the relatively poor modeling of the peak shape at the M point.

Table 2. All Possible Primitive Orthorhombic Models for Phase S in the $2a_p \times 2a_p \times 4a_p$ Cell, Which Allow Simultaneous R_4^+ and M_3^+ Tilt Modes To Be Present along 2 Different Axes

model	s.g.	basis	origin	$^{\$}R_4^+$	$^{\$}M_3^+$	T_4
S-P1	*Pmma*	4 2 2	0, 1/2, 1/2	*a*	*a*	AACC
S-P2	*Pmma*	2 2 4	0, 1/2, 1/2	*c*	*a*	AACC
S-P3	*Pmma*	2 4 2	0, 1/2, 1/2	*a*	*b*	
S-P4	*Pmna*	4 2 2	0, 1/2, 1/2	*a*	*b*	
S-P5	*Pcca*	2 2 4	0, 1/2, 1/2	*c*	*a*	
S-P6	*Pbam*	2 4 2	0, 1/2, 1/2	*c*	*a*	
S-P7	*Pccn*	2 2 4	0, 0, 0	*c*	*a,b,c*	
S-P8	*Pbcm*	2 4 2	0, 0, 0	*a*	*a*	A0C0
S-P9	*Pbcm*	4 2 2	0, 0, 0	*a*	*b*	
S-P10	*Pbcm*	2 4 2	0, 1/2, 1/2	*c*	*a*	
S-P11	*Pbcm*	2 2 4	0, 1/2, 1/2	*a*	*b*	
S-P12	*Pmmn*	2 2 4	0, 0, 0	*c*	*a,b,c*	A0C0
S-P13	*Pmmn*	2 4 2	0, 1/2, 1/2	*a*	*b*	AACC
S-P14	*Pbcn*	2 4 2	0, 0, 0	*a*	*b*	
S-P15	*Pbca*	2 2 4	0, 0, 0	*a*	*b*	
S-P16	*Pnma*	4 2 2	0, 0, 0	*c*	*a,b,c*	
S-P17	*Pnma*	2 2 4	0, 0, 0	*a*	*b*	A0C0

$^{\$}$For simplicity, we have chosen not to use the rigorous 'Order parameter direction' notation (see ref 27). Also, no distinction is intended at this stage between *a* and *b* axes for the R_4^+ and M_3^+ modes; *c* refers to the *c* axis in the 2 2 4 basis, not in the conventional space-group setting shown here (if different). Thus, for example, in model S-P2 there is both a T_4 mode and a R_4^+ mode along the *c* axis and a M_3^+ mode along either *a* or *b*.

requires either unreasonable distortions of octahedra via oxygen-based T modes or unrealistic displacements of cations via the T_5 mode in addition to contributed intensity to unobserved T-line peaks. Trial fits to such models show that the T-line peaks cannot be satisfactorily fit using these models.

Attention was therefore focused on model S-P12. Rietveld refinement commenced by simulating appropriate diffraction patterns by manual adjustment of the relevant distortion modes in ISODISTORT. The key modes used were R_4^+, M_3^+ (for M_3^+ only the two modes around the *a* and *b* axes, with the *c* axis mode fixed at zero initially), and T_4. Applying constraints to the appropriate coordinates in the first instance means that a very good fit can be achieved with only four variable atomic coordinates, corresponding to these tilt modes (model S-P12; Table 1). The fit is significantly better than that of the S-C1 model. At this stage the remaining refinable profile parameters (as for the S-C1 model) and structural parameters could be switched on. Isotropic atomic displacement parameters were constrained according to element type, but all coordinate restraints could be removed in the final stages, leading to a stable and robust refinement, details of which are given in Table 1 (model S-P12a). In fact, only a marginal improvement in fit is achieved in the free refinement, supporting the original premise that the tilt modes are dominant. Note that the refined geometries are all highly reasonable (Nb−O bond lengths in the range 1.96−2.01 Å, O−Nb−O bond angles in the range 85.5−97.0°), and the corresponding Rietveld fit is also excellent. In particular, all key superlattice reflections at the M, R, and T positions are very well accounted for, as seen in the expanded regions in Figure 4. Note, particularly, the correct asymmetric fitting of the M and T peaks. It is important to emphasize that no structural constraints are imposed on the final model: the initial mode constraints were only used to guide the initial stages of refinement. A full mode decomposition analysis was then carried out using ISODISTORT, the results of which are shown in summary form in Table 3 (for full output see Table S1, Supporting Information). It can be seen that the dominant modes are the expected R_4^+, M_3^+, and T_4 modes. However, some significant additional features arise naturally out of the refinement. Most importantly, the dominant M_3^+ mode is around the *b* axis (the 'large' subcell axis), but there is a smaller contribution around both *a* and *c*. Second, there is very little displacement of any of the cations, all being more or less within error bars of their idealized positions. The overall structure is shown in Figure 5, where the true nature of this novel *compound* tilt system (i.e., one in which two *irreps* act simultaneously along one axis) around the *c* axis becomes apparent. In our new notation the tilt system along *c* is approximately '0CAC' (in quotes since, in the case of this compound tilt system, the A and C tilts are no longer constrained to be equal). In Glazer-like notation we may call the tilt system $a^+b^+c^*$ (and in fact close to $a^0b^+c^*$), where c^*

dx.doi.org/10.1021/ic3006585 | *Inorg. Chem.* 2012, 51, 6876−6889

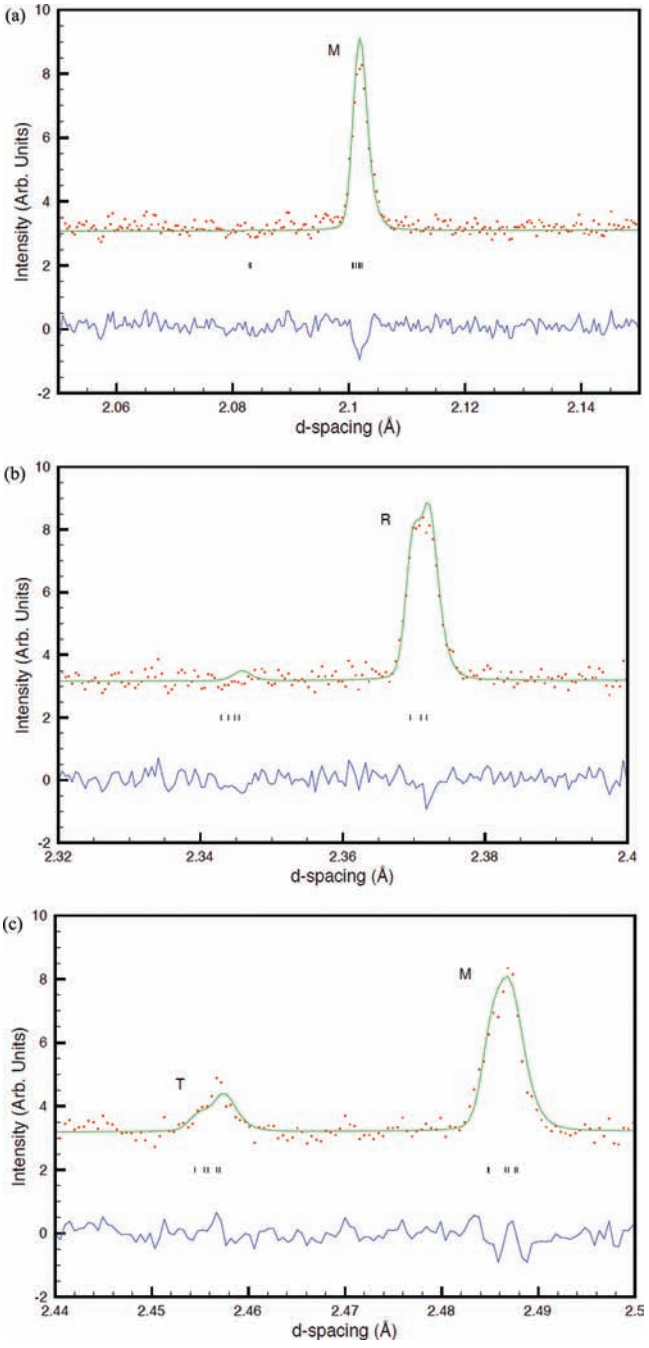

Figure 4. Portions of the Rietveld fit (NPD) to the S-P12a model at 500 °C: (a) M point, (b) R point, and (c) T and M point (compare the fit especially to the M point versus Figure 3).

represents a compound tilt system around the *c* axis, composed of three distinct contributions, the R_4^+, M_3^+, and T_4 modes (or ACAC, CCCC, and A0C0, respectively, in our new notation).

As referred to above, we should also consider the possibility that the major tilt modes R_4^+, M_3^+, and T_4 are present along three *different* axes. Models S-P13 or S-P17 in Table 2 allow this (but without the additional subtlety of more than one M_3^+ mode). Model S-P17 was therefore tested, first applying approximate values of the three tilt modes but eventually allowing a full refinement of all 31 coordinate variables (Table 1). Although the overall level of fit, as judged by χ^2, is almost as good as that of model S-P12a (as shown in the Figure S4, Supporting Information) the positioning of the T_4 peak is

Table 3. Symmetry Mode Analysis (summary only) for the Final Phase S Model (S-P12a)[a]

mode	A(s) (overall)	d(max)		A(s)	d(max)
Δ_1	0.19(7)	0.042(7)			
Δ_2	0.29(3)	0.072(7)			
R_4^+	**1.12(3)**	**0.198(5)**			
R_5^+	0.13(9)	0.03(2)			
X_1^+	0.04(3)	0.007(2)			
X_5^+	0.23(6)	0.040(7)			
M_3^+	**1.14(3)**	**0.189(5)**			
			M_3^+ (*c* axis)	−0.36(3)	0.064(5)
			M_3^+ (*a* axis)	0.19(3)	0.034(5)
			M_3^+ (*b* axis)	**1.07(3)**	**0.189(5)**
M_4^+	0.14(3)	0.019(5)			
T_3	0.04(9)	0.008(8)			
T_4	**0.62(3)**	**0.155(8)**			
Z_4	0.49(3)	0.092(11)			

[a]See ref 27 for definitions of A(s) and d(max).

inferior. This effect is extremely subtle but is certainly within the resolution limits of HRPD. This means that the R_4^+ and T_4 tilt modes must both occur relative to the 'medium' axis, thus confirming that the R_4^+ and T_4 tilts are, in fact, required to be *simultaneously* along the *c* axis.

In summary, the process for elucidating the final model for phase S is as follows: (i) Indexing of key superlattice peaks and their assignment to M, R, and T points. (ii) An assumption that the M- and R-point reflections are, at least in part, due to octahedral tilt modes (M_3^+ and R_4^+, respectively). (iii) Exhaustive ISODISTORT search for all possible models incorporating at least these two tilt modes, within the scope of the cell metrics discussed and centrosymmetric tetragonal or orthorhombic symmetries. (iv) Discrimination of these potential models based on details of peak positions and peak splittings, in particular, including unambiguous assignment of the M_3^+, R_4^+, and T_4 tilt modes to the appropriate unit cell axes.

We ultimately conclude that model S-P12a in Table 1, space group *Pmmn*, is the *unique* choice for the structure of phase S. A full representation of the Rietveld fit to this model is shown in Figure S5, Supporting Information.

Phase R at 440 °C. Inspection of the raw data from both NPD and SXPD experiments in the range range $2.0 < d < 2.5$ Å shows similarities but distinct differences as compared to phase S. The differences suggest a $6a_p$, rather than $4a_p$ cell repeat along one axis, with key superlattice peaks at the R, M, and T points, labeled in Figure 6. Interestingly, there are two distinct sets of T points at (1/2, 1/2, 1/3) and (1/2, 1/2, 1/6) allowed in such a unit cell. Only the former are observed (i.e., with $l = 2n$, whereas $l = 2n + 1$ peaks are absent), implying that the T mode in itself only triples the unit cell along *c*. As will be seen, the additional doubling arises from the simultaneous R_4^+ tilt mode. There are four distinct T_4 tilt modes possible in unit cells of this type, two of which correspond to the (1/2, 1/2, 1/3) point and two to the (1/2, 1/2, 1/6) point. These modes are designated A0CA0C, A^2CCA^2CC and A0CC0A, A^2ACC^2CA, respectively (Figure 7 and Figure S6, Supporting Information). The meaning of A, C, and 0 has been described previously; 'A^2' and 'C^2' are used to described anticlockwise and clockwise tilts, respectively, which are exactly *twice* (i.e., symmetry imposed) those for A and C. Although these diffraction patterns unambiguously require a $6a_p$ repeat along one direction, the

dx.doi.org/10.1021/ic3006585 | *Inorg. Chem.* 2012, 51, 6876−6889

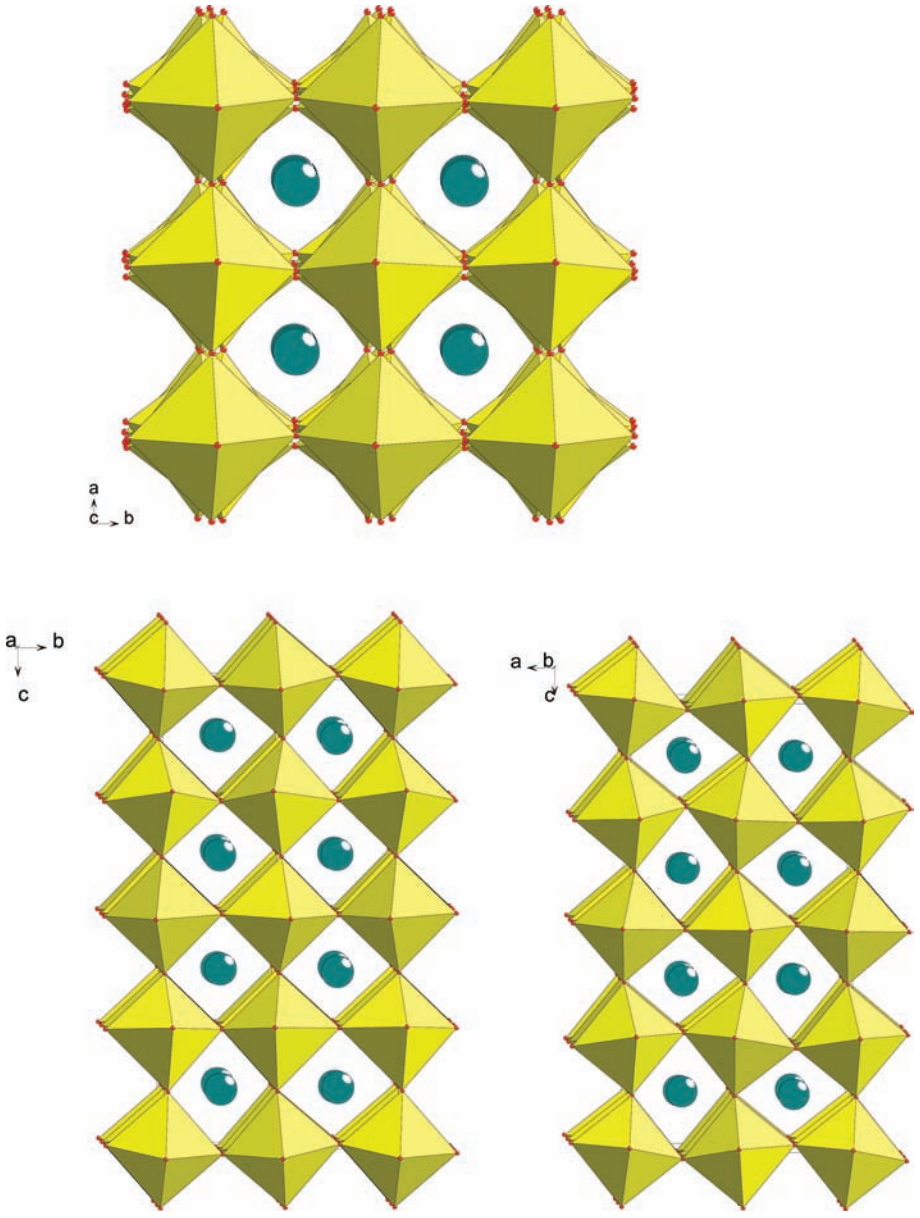

Figure 5. Final crystal structure of phase S, *Pmmn* model (S-P12a): (a) *c* axis, showing compound tilt system comprising superposed M_3^+, R_4^+, and T_4 modes, (b) *a* axis, showing the small M_3^+ mode, and (c) *b* axis, showing the larger M_3^+ mode.

choice between tetragonal $\sqrt{2}a_p \times \sqrt{2}a_p \times 6a_p$, primitive orthorhombic $\sqrt{2}a_p \times \sqrt{2}a_p \times 6a_p$ and *C*-centered orthorhombic $2a_p \times 2a_p \times 6a_p$ is less obvious, due to the lack of clear peak splittings or shoulders.

An initial trial model (R-T1) could once again be generated from ISODISTORT in tetragonal space group *P4/mbm*. Focusing solely on the NPD data first, this model fits the intensities of the observed superlattice features reasonably based on the R, M, and T(1/3) modes described above. However, in more detailed plots it can be seen that the positions of the superlattice peaks are poorly fit, for example, the T- and M-point peaks in the region $d = 2.35-2.5$ Å (Figure S7, Supporting Information). More flexibility is required in the model to describe these peaks adequately. Following an analogous procedure to that described for phase S, ISODISTORT simulations were carried out in both primitive orthorhombic $\sqrt{2}a_p \times \sqrt{2}a_p \times 6a_p$ and *C*-centered orthorhombic $2a_p \times 2a_p \times 6a_p$ superlattices (point group *mmm* only in both cases). For each of these cell choices ISODISTORT lists 40 possible models, of which only two, in each case, have the necessary presence of simultaneous R_4^+ and M_3^+ tilt modes (Table 4). One of the $T_4(1/3)$ tilt modes also occurs in each of these options.

At this stage, attention was switched temporarily to analysis of the SXPD data. First, a test for the nature of the orthorhombic distortion was carried out in the same style as for phase S by lowering the symmetry of the refined *P4/mbm* model to either of the two orthorhombic $\sqrt{2}a_p \times \sqrt{2}a_p \times 6a_p$ options R-P1 or R-P2, with appropriate R-, M-, and T-point tilts built in to the starting model. Again, this gives unsatisfactory, incompatible splittings of the $(111)_p$ and $(200)_p$ reflections. However, more significantly, it does not reproduce the M peaks near $d \approx 2.48$ Å very well: this is a doublet, the splitting of which leads to a similar splitting of the $(111)_p$. This can be seen much more clearly in the SXPD data, where the somewhat enhanced resolution clearly resolves the

dx.doi.org/10.1021/ic3006585 | *Inorg. Chem.* 2012, 51, 6876−6889

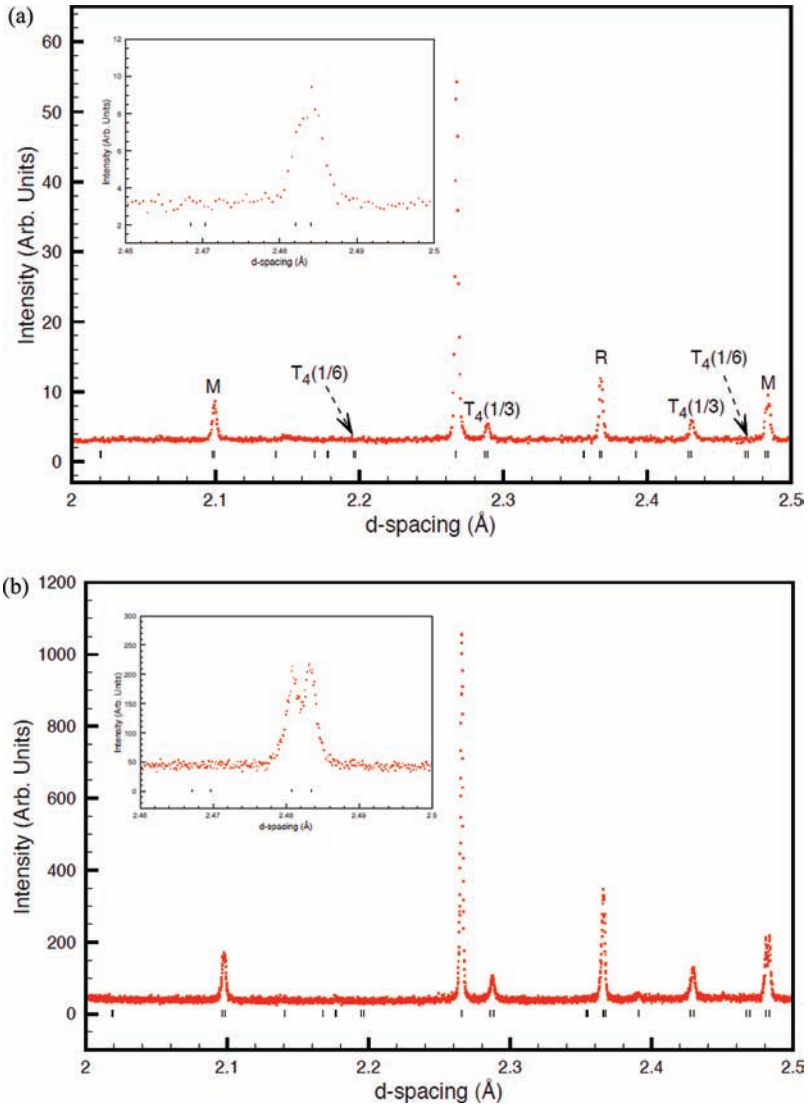

Figure 6. Portions of the raw diffraction data for phase R at 440 °C showing superlattice peaks at the M, R, and T points: (a) NPD and (b) SXPD data. (Insets) Expansion of the M-point peak splitting.

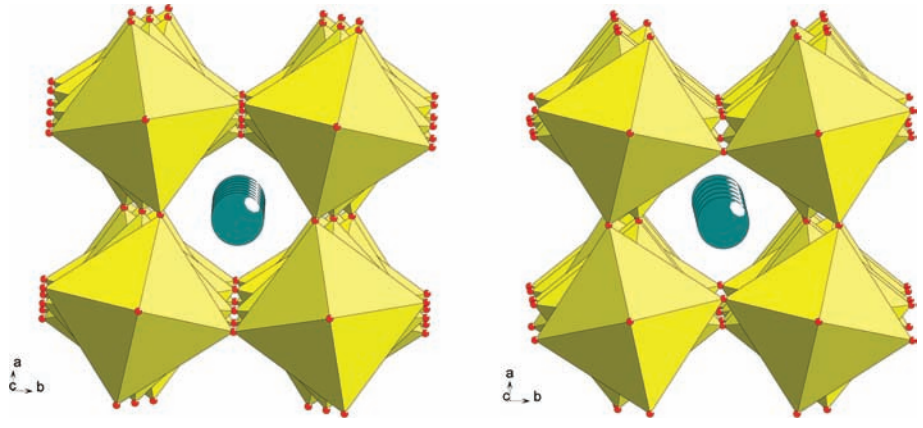

Figure 7. Tilt modes of the two possible T_4 (1/2, 1/2, 1/3) *irreps* that can operate in a $2a_p \times 2a_p \times 6a_p$ orthorhombic supercell: (a) A0CA0C and (b) A^2CCA^2CC (the two T_4 (1/2, 1/2, 1/6) modes are shown in Figure S6, Supporting Information).

M-point splitting (Figure 6; Figure S8, Supporting Information). This convincingly rules out the $\sqrt{2}a_p \times \sqrt{2}a_p \times 6a_p$ superlattice options. Hence, we are left with the two *C*-centered $2a_p \times 2a_p \times 6a_p$ superlattices, R-C1 and R-C2. However, there is now an incompatibility between the splittings of the T and M peaks, again seen more clearly in the SXPD data (Figure S9, Supporting Information). The inescapable conclusion is that, once again, the symmetry must be reduced to a primitive

dx.doi.org/10.1021/ic3006585 | *Inorg. Chem.* 2012, 51, 6876−6889

Table 4. Models Considered for Phase R in the $\sqrt{2}a_p \times \sqrt{2}a_p \times 6a_p$ and $2a_p \times 2a_p \times 6a_p$ Cells As Discussed in the Text[a]

model	S.G.	basis	origin	R_4^+	M_3^+	T_4
R-T1	*P4/mbm*	$\sqrt{2}$ $\sqrt{2}$ 6	0, 0, 0	*c*	*c*	A^2CCA^2CC
R-P1	*Pbam*	$\sqrt{2}$ $\sqrt{2}$ 6	0, 0, 0	*c*	*c*	A^2CCA^2CC
R-P2	*Pnma*	$\sqrt{2}$ 6 $\sqrt{2}$	0, 0, 0	*ab*	*c*	A^2CCA^2CC
R-C1	*Cmcm*	2 2 6	1/2, 1/2, 0	*a*	*c*	A^2CCA^2CC
R-C2	*Cmmm*	2 2 6	−1/2, 1/2, 0	*c*	*c*	A^2CCA^2CC
R-P3	*Pmmn*	2 6 2	0, 0, 0	*a*	*a,b,c*	A^2CCA^2CC
R-P4	*Pnma*	2 2 6	0, 1/2, 1/2,	*a*	*b*	A0CA0C

[a]Note: The simplified axial notation of Table 2 is also used here.

orthorhombic cell, in this case $2a_p \times 2a_p \times 6a_p$. This is also the simplest way to allow R-, M-, and T-point tilts to occur along three mutually exclusive axes which, this time, *is* necessary to explain fully the observed superlattice peak positions/splittings. For example, the splitting of the M-point reflections near d = 2.48 Å necessitates the dominant M_3^+ mode to be oriented along the axis with the 'middle' of the three a_p values. Extension of this to analysis of the R_4^+ and T_4 splittings leads to an unambiguous assignment of the three subcell axes as 'small', 'medium', and 'large', despite the fact that these axial lengths differ once again by only about 0.1%. ISODISTORT produces 272 possible space groups/settings for $2a_p \times 2a_p \times 6a_p$ orthorhombic (*mmm* point group) unit cells, in direct parallel to those found for phase S. A systematic search through all these options reveals only two candidate space groups: *Pmmn* and *Pnma* (models R-P3 and R-P4, Table 4).

These two models display the two different $T_4(1/3)$ tilt modes and also permit different secondary cation displacement and octahedral distortion modes. Idealized starting models for R-P3 and R-P4 were derived from ISODISTORT by adjusting the three mutually perpendicular R_4^+, M_3^+, and T_4 tilt modes to values that reproduced the observed reflection intensities approximately. We note at this stage that none of the possible T modes associated with Na or Nb displacements adequately model the observed T-point peaks acting alone. In other words, these must at best be secondary contributors to the primary T_4 oxygen tilt mode.

For preliminary analysis and comparison of these two models the SXPD data alone were used. The refinement strategy was kept as simple as reasonably possible. To refine the structure solely in terms of the three primary octahedral tilt modes, corresponding structural constraints were imposed such that the structures were described with only three variable atomic coordinates (grouped) rather than the 49 or 51, respectively, that a full refinement in models R-P3 or R-P4 would require. These two refinements (R-P3a and R-P4a) gave indistinguishable fits, as shown in Table 5. Adding in all the refinable cation coordinates as free variables led to marginal improvements in both cases, but again, there was no way to distinguish between the two models (R-P3b, R-P4b). Attention was therefore once again switched to the NPD data. In addition, some joint refinements of both data sets simultaneously were explored: although these were stable, due to slight temperature offsets between data sets, they are not reported in detail.

Now, a marginally better fit could be discerned with the R-P3 models over the R-P4 models. Moreover, the R-P3 refinements (either constraining the tilt modes but allowing free refinement of the cation positions or allowing a full unconstrained refinement) were always robust and stable, whereas the R-P4

Table 5. Comparative Refinements for Phase R at 440 °C in the Primitive Orthorhombic Models Discussed in the Text[a]

model	space group	N_{xyz}	N_{ref}	χ^2
R-P3a	*Pmmn*	49	3	2.08
R-P4a	*Pnma*	51	3	2.08
R-P3b	*Pmmn*	49	21	2.07
R-P4b	*Pnma*	51	24	2.07
R-P3c	*Pmmn*	49	21	1.76
R-P4c	*Pnma*	51	24	1.97
R-P3d	*Pmmn*	49	49	1.69
R-P4d	*Pnma*	51	51	1.76

[a]N_{xyz} is the number of allowed variable atomic coordinates; N_{ref} is the number actually refined, taking into account constraints imposed by the tilt modes. Isotropic atomic displacement parameters were grouped by element type, and the same set of profile parameters was refined in each case. 'a' models: tilt modes only, X-ray data only. 'b' models: 'tilts' plus all cation coordinates free, X-ray data only. 'c' models: as 'b', but NPD data only. 'd' models: all coordinates refined freely, NPD data only. The refined unit cell parameters for model R-P3c are a = 7.85371(6) Å, b = 23.54619(19) Å, c = 7.85677(7) Å.

refinements typically failed to converge consistently. Table 5 shows two comparative fits to the NPD data for partially constrained (R-P3c, R-P4c) or free (R-P3d, R-P4d) models. It can be seen that there is only a relatively small improvement on allowing full flexibility of the structure; moreover, there were instabilities in some refinements, caused largely by erratic Na cation displacements. The differences between the Rietveld agreement factors in themselves are insufficient to draw a definitive preference for the R-P3 versus R-P4 models. These comparisons were extended to a wider temperature range within the phase R regime (Table S2, Supporting Information). In each case, the R-P3c model gives a better fit than the R-P4c, but when the constraints are removed fully the R-P3d and R-P4d models give extremely similar levels of fit. In order to test the validity of these various models further, ISODISTORT was used for a full mode decomposition analysis. In addition, DFT calculations were undertaken for each model.

The two final structural models (R-P3c and R-P4c) for phase R are shown in Figure S10, Supporting Information, portions of the final Rietveld fits in Figure 8 and Figure S11, Supporting Information, and full Rietveld fits in Figure S12, Supporting Information. A breakdown of these two structures into their constituent modes is given in Table 6 and Table S3, Supporting Information. As can be seen, the three principle modes are the R_4^+, M_3^+, and T_4 tilts (note that we have chosen the conventional setting of the space group *Pmmn*, which requires *b* rather than *c* as the $6a_p$ axis). Using the new notation introduced above, the respective T_4 modes are described as A^2CCA^2CC and A0CA0C or in adapted Glazer notation the full tilt symbols are $a^+b^*c^-$ (b* = A^2CCA^2CC) and $a^-b^+c^*$ (c* = A0CA0C). A comparison of the mode decompositions using the various different models in Table 5 shows that the principal tilt modes are reliably determined in each case regardless of the details of the model or which data set(s) are used, whereas the details of the much smaller cation displacement modes are, not surprisingly, less well determined.

In summary, for analysis of phase R, a procedure directly analogous to that used for phase S was used: a $6a_p$ rather than a $4a_p$ supercell was found and, once again, octahedral tilt modes were shown to be largely responsible for the superlattice peaks at each of the R, M, and T points. The availability of single-phase SXPD data aided in identifying unambiguously the

dx.doi.org/10.1021/ic3006585 | *Inorg. Chem.* 2012, 51, 6876−6889

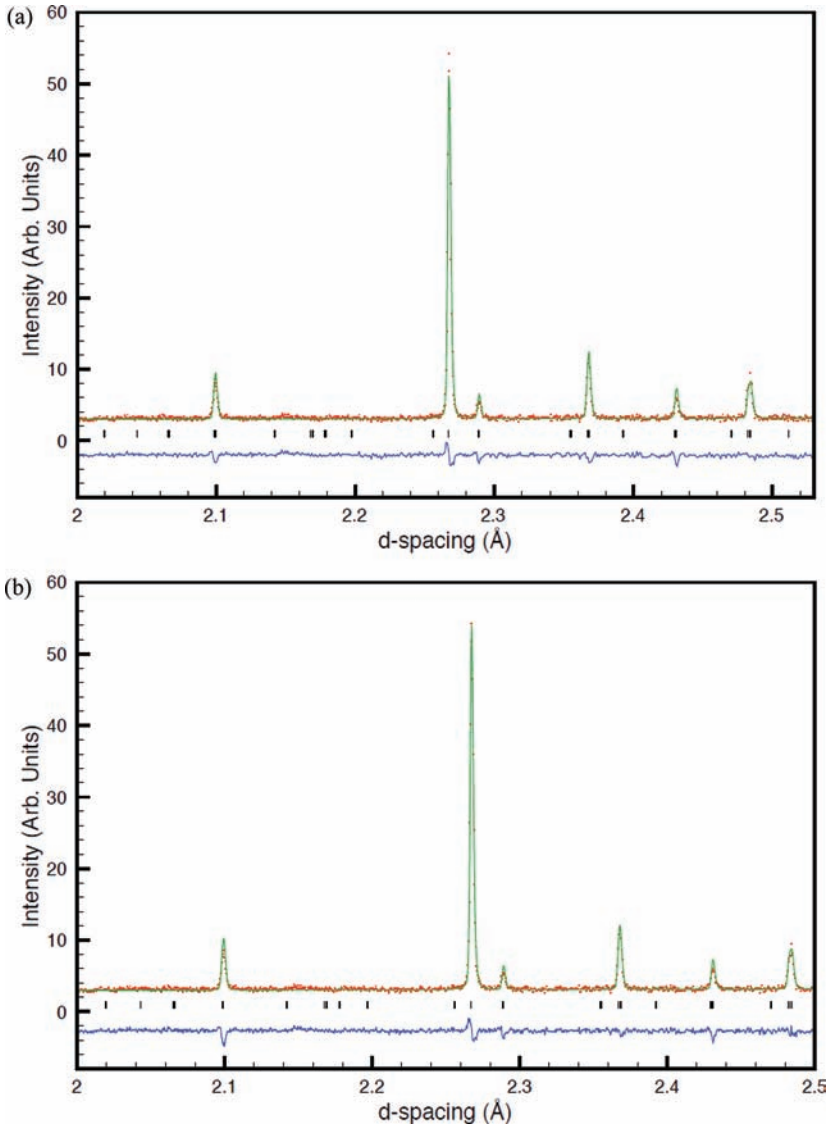

Figure 8. Portion of the Rietveld fits (NPD) for phase R at 440 °C: (a) R-P3c model and (b) R-P4c model.

orientation of the various tilt modes relative to the subcell axes. Nevertheless, it proved impossible to suggest a preference for either of the two competing final models from the present powder diffraction data alone.

Phase Evolution Versus *T*. Refinements of all the NPD data sets throughout the region 340 °C < *T* < 530 °C allowed the detailed evolution of the structure to be tracked from phase P through phases R and S and into phase T1. For these refinements, the models used were the standard models for phase P[14] and T1,[16] the fully unconstrained model S-P12 (Table 2) for phase S, and the partially constrained model R-P3c (Table 5) for phase R. In particular, trends in lattice parameters are very well determined (Figure 9), but also there is sufficient data to allow trends in the tilt modes through phase R to be followed (Figure S13, Supporting Information); all three tilt modes show a reduction with increasing temperature with the T_4 mode showing the largest effect. Evolution of the lattice parameters agrees remarkably well with the early work of Megaw et al.[3,6] Inclusion of the point at 340 °C corresponding to phase P highlights how subtle the deviations from pseudocubic lattice metrics are through phases R and S. The subtleties of the phase transitions through the R → S and S → T1 regions are further emphasized by the plot of unit cell volume per formula unit (Figure S14, Supporting Information). The anisotropic thermal expansion behavior through phase R is presumably correlated with the anisotropic reductions in the octahedral tilt modes in this region.

■ DISCUSSION

There have been several previous studies of the high-temperature phase diagram of $NaNbO_3$ over the past 40 years or so, commencing with the pioneering work of Megaw and co-workers.[3−8] Several suggestions of possible unit cell metrics and/or space groups have been given for phases R and S, and several full structural models have been suggested. These are summarized in Table 7. We believe that the present structural model for phase S is unambiguous, and our analysis provides two models for phase R, which are very difficult to distinguish from the present study. Therefore, it is of interest to take a closer look at previous models to see if there are elements in common with our own conclusions.

For phase S, Ahtee et al.[6] suggested a $2a_p \times 2a_p \times 2a_p$ supercell with Glazer tilt system $a^-b^+c^+$ based on single-crystal X-ray data. A full refinement was not carried out, and an

dx.doi.org/10.1021/ic3006585 | Inorg. Chem. 2012, 51, 6876−6889

Table 6. Symmetry Mode Analysis (summary only) for the Final Phase R Models (R-P3c and R-P4c), and a Comparison to the Sakowski-Cowley Model (ref 4)[a]

	R-P3c-*Pmmn*		R-P4c-*Pnma*		S-C model (ref 4)
mode	*A*(s) (overall)	*d*(max)	*A*(s) (overall)	*d*(max)	*A*(s) (overall)
Δ_1	0.20(14)	0.05(3)	0.30(20)	0.07(5)	0.04
Δ_2	0	0	0	0	0
Δ_5	0.21(14)	0.06(4)	0.24(12)	0.06(3)	**0.35**
R_4^+	**1.372(2)**	**0.1980(3)**	**1.330(2)**	**0.1920(3)**	**1.33**
R_5^+	0.11(7)	0.02(1)	0.03(13)	0.01(3)	0.03
X_1^+	0.04(15)	0.01(3)			0
X_5^-			0.06(8)	0.01(1)	
X_5^+	0.10(11)	0.018(6)	0.09(13)	0.02(3)	0.13
M_2^-			0.1(2)	0.02(4)	
M_3^+	**1.510(3)**	**0.2179(4)**	**1.574(3)**	**0.2272(4)**	**1.56**
M_4^+	0	0	0	0	0.32
M_5^-			0.1(2)	0.02(4)	
T_3	0.02(14)	0.00(3)	0.1(2)	0.02	0
T_4	**1.212(5)**	**0.247(1)**	**1.151(6)**	**0.204(1)**	**0.51**
T_5	0.27(13)	0.08(4)	0.18(14)	0.03(4)	0.27
Z_1	0.25(11)	0.06(4)	0.24(10)	0.06(3)	0
Z_2	0.37(14)	0.11(4)	0.24(13)	0.07(4)	0.18
Z_4	0.13(14)	0.03(3)	0.12(14)	0.025	0.27

[a]Note: The S−C model adopts the same Isotropy subgroup as our R-P3c model. See Table 7, and compare Table S3a, Supporting Information. The appearance of several 'zero amplitude' modes merely shows that the model was not fully refined and is of no serious consequence.

Table 7. Previous Models Proposed for Phases R and S[a]

phase	basis	origin	space group	key modes	ref
R	2 6 2	0, −1, 0	*Pmmn*	$M_3^+(a,b)$, $T_4(b)$, $R_4^+(c)$, Δ_5 (Na, Nb)	4
R	2 4 6				19
R*	2 2 2	1/2, 1/2, 0	*Pmmn*	$R_4^+(c)$, $M_3^+(a)$, $M_3^+(b)$	21
R	$\sqrt{2}$ $\sqrt{2}$ 6	1/2, 1/2, 0	*Pbnm*	$M_3^+(c)$, $T_4(c)$, $R_4^+(ab)$	22
S	2 2 2	0, 0, 0	*Pnmm*	$R_4^+(a)$, $M_3^+(b)$, $M_3^+(c)$	6
S	2 4 6				19
S	$\sqrt{2}$ $\sqrt{2}$ 12	0, 0, 0	*Pbnm*	$M_3^+(c)$, $T_4(c)$, $R_4^+(c)$	22

*This phase is derived from heating a sample of (predominantly) phase Q, so may be a genuinely different phase: it is essentially the same model as the Ahtee model for phase S. [a]Note that that the letters in brackets represent the axial directions of the tilt modes in the crystal structure in the setting presented. They are not formal 'Order parameter directions' (see ref 27).

assumption was made that the Nb atoms are undisplaced. This model identifies both M_3^+ and R_4^+ tilt modes to be present but misses the additional more subtle T_4 tilting and the consequent $4a_p$ superlattice. Darlington and Knight[19] used NPD data (HRPD) and suggested both phases R and S to have much more complex supercells, based on the observation of very weak additional reflections. These are not evident in the present work, and we suggest that their misassignment of the correct unit cell metrics for both phases is apparently caused by observing a coexistence of the two phases, as shown in the Figure S15, Supporting Information. Mishra et al.[22] recently suggested new models for both phases based on NPD. In both cases they suggest a $\sqrt{2} \times \sqrt{2}$ metric in the *ab* plane. For phase S a curious $12a_p$ supercell is suggested, whereas for phase R the correct $6a_p$ supercell is proposed. This study suffers from poor resolution in the NPD data which, given the very subtle nature of the distortions away from metrically tetragonal symmetry for both phases described above, must preclude a satisfactory unit cell determination. Although some of the correct tilt modes are incorporated in these models, the correct axial directions are missed, and some of the suggested displacive/distortive modes give rise to unrealistic geometries.

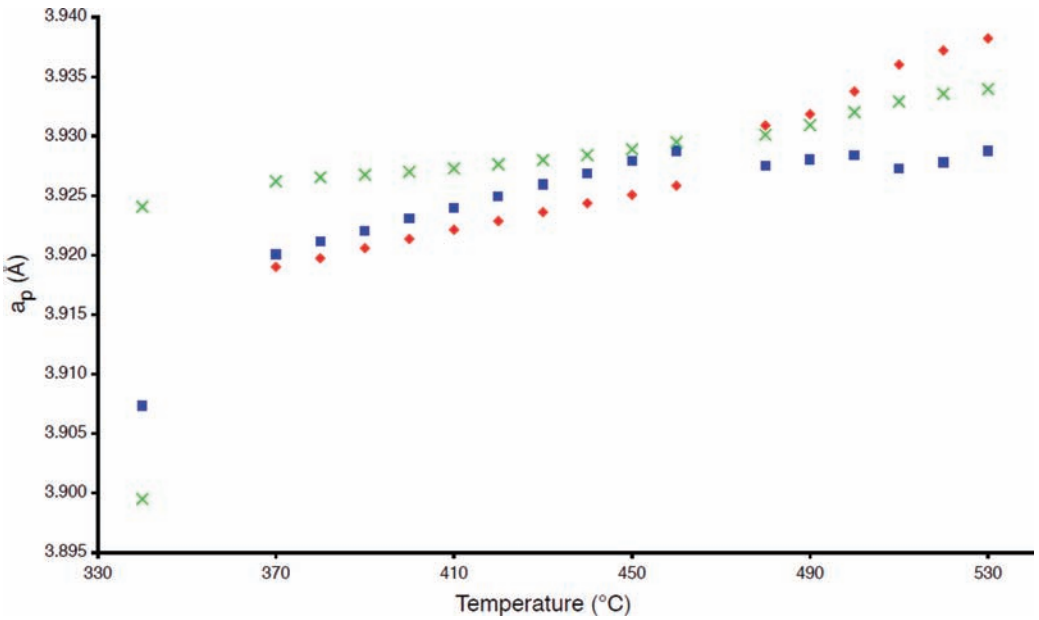

Figure 9. Trends in lattice parameters through phases T1, S, R, and into P. Note that these are normalized to the aristotype metric and plotted relative to the principal tilt modes along resulting 'small', 'medium', or 'large' axes rather than relative to the axes assigned in the refinement models. In this way the principal modes can be followed: diamonds, M_3^+, crosses, R_4^+, squares, other (see also Figure S14, Supporting Information).

dx.doi.org/10.1021/ic3006585 | *Inorg. Chem.* 2012, 51, 6876−6889

The most meticulous of the previous studies is the model for phase R described in ref 4, obtained by single-crystal XRD. This is a remarkable piece of work for such an 'early' date and correctly identifies the cell metrics for phase R confirmed in the present work. Moreover, the final model proposed (although unrefined) actually corresponds very closely to our own R-P3 model! Sakowski-Cowley's deduction of this model was based primarily on the fitting of key superlattice peaks to antiferroelectric Nb displacements rather than to octahedral tilts (the work precedes Glazer notation). Nevertheless, it does ultimately derive the A^2CCA^2CC T_4 tilt system we propose. The main difference between the two models is that Sakowski-Cowley slightly underestimates the magnitude of the T_4 tilt (Table 6, Figure S16, Supporting Information); the degree of agreement between the two studies for the magnitudes of the R_4^+ and M_3^+ modes is remarkable. The Δ_5 Nb displacements on which their trial model is based are arguably also observable in our models (albeit with very small amplitudes). The minor differences should not detract from the essential agreement of Sakowski-Cowley's original model with our own model R-P3.

In order to gain further insight into the suitability of the models proposed single-point energy DFT calculations were performed on a number of phases of $NaNbO_3$ using structures obtained either from the ICSD (refs 6 and 14) or from refinements within this work (phases P, R, S, and T1). Geometry optimizations were also performed on all structures by allowing (i) atomic coordinates only to vary and (ii) atomic coordinates and lattice parameters to vary. Energies are expressed in eV per formula unit of $NaNbO_3$.

Figure 10 shows the energies of the phases as determined by DFT from structures derived entirely from diffraction. It can be

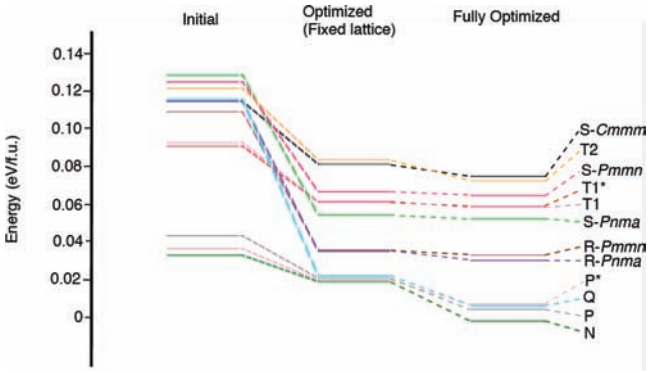

Figure 10. Calculated energies of various phases of $NaNbO_3$ for both initial and optimized structures. Labels P and T1 refer to models from the present work, and labels P* and T1* refer to the literature models (refs 14 and 16, respectively). Energies are quoted relative to the lowest energy (fully optimized) phase N. Dashed lines are a guide-to-the eye only.

seen that the low-energy structures correspond to the phases (N, P, and Q) observed at low/room temperature experimentally, although the order of phases observed at higher energies does not reflect exactly the experimentally observed phase variation with temperature. Of course, it should be noted that the energy quoted here is the internal energy ΔU, whereas phase stability in experiment is concerned with variations in ΔG, i.e., including a consideration of entropy and temperature/vibrational effects. While it may be possible to include such corrections, in principle, this is far too complicated and costly a calculation to be undertaken here. Furthermore, the calculations reveal relatively large forces (>1 eV/Å) upon atoms in a number of these initial (i.e., unoptimized) structures, indicating some error or uncertainty in the exact atomic coordinates. For example, in the phase P model proposed by Sakowski-Cowley[14] there are forces of up to 2.30 eV/Å in one direction and 0.85 eV/Å along another. In contrast, the model for phase P obtained directly from refinement of NPD data in this work exhibited forces of 0.57 eV/Å. It should be noted, however, that the models considered for phases R and S (R-P3, R-P4, S-C1, S-P12, and S-P17) and phase T1 appear to have very similar energies. In general, the models for phase R have a lower energy than those for phase S, consistent with its observation at lower temperatures in experiment. It is not possible to say, however, that one of the candidate models for phase R or S is favored over any other.

In a subsequent step, models were then geometry optimized using DFT with atomic coordinates varied in order to minimize the forces upon the atoms, although initially lattice parameters were kept fixed. (It should be noted that small overestimation of unit cell lengths and bond lengths is common when using DFT calculations owing to the inaccuracies in the GGA functional employed; this effect can be minimized if the unit cell parameters are constrained). After optimization forces upon the atoms were ~0.05 eV/Å. As shown in Figure 10, although the exact energies change upon optimization (owing to small changes in the atomic positions), the relative energies change relatively little, with phases N, P, Q still being lowest in energy (although the energy difference between these three has decreased). There are small changes in the energy of the high-temperature phases with a lowering of the energy of phase R relative to T1, in better agreement with the order of the phases observed as a function of temperature experimentally. In general, the changes in the structures upon optimization were extremely small, and the NbO_6 octahedral tilt systems did not change (confirmed by comparing the three main tilt modes (M_3^+, R_4^+, and T_4) using ISODISTORT). However, there were two notable exceptions to this; for the *Pmmn* models for phase R (R-P3) and phase S (S-P12) significant changes were observed, resulting in a final model closely resembling phase N (*R*3*c*). The 6- or 4-unit repeat tilt system became an 'AC' tilt system (Figure S17, Supporting Information), and there were pronounced distortions in the NbO_6 octahedra with a change in the bond lengths (between 1.984 and 1.992 Å initially) to the three 'short' and three 'long' bonds (typically three in the range 1.87−1.91 Å and three in the range 2.08−2.16 Å) characteristic of those associated with the rhombohedral phase. This suggests that although the observed phases may represent a minimum in ΔG, they are not a minimum in ΔU and perhaps could be stabilized by high-temperature vibrations. After optimization calculated energies for the R-P3 (local minima) and R-P4 models are very similar with neither model particularly favored. The energy differences between the three models for phase S have increased slightly, but the three are still too similar to draw any unambiguous conclusions, particularly given the lack of any vibrational corrections.

Full geometry optimization (i.e., with variation of the lattice parameters) of all structural models was also undertaken to enable any limitations imposed by the refinement to be overcome. After optimization, (i) all models for phase P (i.e., those from different initial structures) are of equal energy and are of slightly higher energy than the ferroelectric phase Q (the two often occur as phase mixtures in room temperature synthesis), (ii) phase T2 is the highest in energy (the high-

dx.doi.org/10.1021/ic3006585 | *Inorg. Chem.* 2012, 51, 6876−6889

temperature phase in experiment), and (iii) R-P3 and R-P4 are very similar in energy and lower in energy than phases S, T1, and T2, in agreement with the phase variation observed with temperature in experiment. As seen above, the range of energies observed for the proposed models for phases R and S are very small, and it is not possible to rule out any model as a possibility or to unambiguously assign any model as correct purely using DFT calculations. As a general conclusion from these calculations, however, it is noticeable that there are many possible forms of $NaNbO_3$ with similar energy, supporting the rich polymorphism observed experimentally and the presence of mixed phases from different synthetic approaches. In order to fully understand the higher temperature phases in particular it would be necessary to include some effects of temperature and vibrational corrections, which, although beyond the scope of the present work, does offer an intriguing possibility for the future.

A full summary of the 'seven phases' of $NaNbO_3$, with their dominant distortion modes, is given in Table 8. The sequence

Table 8. "Seven phases of $NaNbO_3$", Updated To Include Proposed Models from the Present Work and Highlighting the Principal Distortion Modes Present in Each

phase	space group	*small*[a]	*medium*[a]	*large*[a]	ref
U	$Pm\bar{3}m$				
T2	*P4/mbm*			$c\ M_3^+$	15
T1	*Cmcm*	$a\ 0$	$b\ R_4^+$	$c\ M_3^+$	6
S	*Pmmn*	$a\ (M_3^+)$	$c\ R_4^+\ T_4$	$b\ M_3^+$	this work
R	*Pmmn*	$a\ M_3^+$	$b\ T_4$	$c\ R_4^+$	this work
	Pnma	$b\ M_3^+$	$c\ T_4$	$a\ R_4^+$	this work
P	*Pbcm*	$a\ R_4^+$ $\Delta_5(Na,Nb)$	$c\ T_4$	$b\ R_4^+$ $\Delta_5(Na,Nb)$	14
N	*R3c*	$R_4^+\ \Gamma_4^-$	$R_4^+\Gamma_4^-$	$R_4^+\Gamma_4^-$	13

[a]*Small*, *medium*, and *large* refer to the relative magnitudes of the pseudocubic subcell axes, a_p; *a*, *b*, and *c*, refer to the crystallographic axes in the actual setting used: for example, in phase T1the medium subcell axis is *b*, and this is the direction of the R_4^+ tilt mode. Note that the details of the T_4 modes differ between the different phases. The Δ_5 and Γ_4^- modes are cation displacements.

of transitions at the higher temperature end of the series is dominated by successive octahedral tilt modes, as anticipated in the early work of Megaw et al.[3,4] The two dominant modes are the simple M_3^+ and R_4^+ in-phase and antiphase tilts, respectively, which are introduced at the U → T2 and T2 → T1 transitions and remain down to phase R, although with varying axial orientations. The structural frustration inherent in this system is emphasized, however, by the additional occurrence of more complex tilts along the T line in phases S, R, and P, which produce supercell repeats of $4a_p$, $6a_p$, and $4a_p$, respectively, which cannot be described within the Glazer notation. There is no evidence for significant cation displacements in the highest temperature phases, but very small antiferroelectric Nb displacements are present in phase R, as suggested by Megaw et al. These displacements become much more significant on lowering the temperature into phases P and N. In phase N, the cation modes dominate and $NaNbO_3$ ultimately becomes ferroelectric. It is interesting to note that there is a preference for purely in-phase (M_3^+) tilts in phase T2 and purely out-of-phase (R_4^+) tilts in phase N: the peculiar behavior seen in the intermediate phases might be regarded as a competition between these two contradictory modes with consequent frustration leading to the observed complexity.

The complex tilt systems we propose for phases S and R are new and unique. In phase S, in particular, it is of interest as it contains two different *irreps* of very significant magnitude along a single crystallographic axis, i.e., simultaneous R_4^+ and T_4 modes along *c*. Note that in phase P[33] the $4a_p$ axis originates from a single T_4 mode (AACC) which, in principle, can keep all the octahedra perfectly regular; this is impossible for a *compound* tilt system such as that in phase S. Such compound tilt systems were not *explicitly* considered in Glazer's original scheme (but, in fact, certain examples arose naturally from that analysis, and these are discussed further in ref 25). There have been very few previous characterisations of compound tilts, though they are allowed in some low-symmetry systems and have significant magnitudes in examples such as $BiNiO_3$[34] and WO_3 ($P\bar{1}$ polymorph).[35,36] No attempt been made to classify these tilt systems. In fact, the simplest type, involving simultaneous M_3^+/R_4^+ tilts around one axis, can be accommodated in a supercell of only $\sqrt{2}a_p \times \sqrt{2}a_p \times 2a_p$, but it is not possible to keep the octahedra strictly identical, and so this system does not fit into the Glazer scheme (Figure S18, Supporting Information). Such a tilt system $a^0a^0c^*$ (c^* = '0C') could, in principle, produce a diffraction pattern very similar to that of phase T1, but the two models are easily distinguishable in this case due to the relatively large differences in the dimensions of the three crystallographic subcell axes.

CONCLUSIONS

In summary, we carried out a very detailed analysis of the high-temperature phase behavior of $NaNbO_3$ using a combination of high-resolution neutron and X-ray powder diffraction coupled with systematic symmetry-mode analysis and supported by DFT calculations. New structural models have been proposed for the elusive phases S (stable between 480 and 510 °C) and R (370−470 °C). We limited our considerations to centrosymmetric models of symmetry no lower than orthorhombic: this provides models that fit the available data extremely well, although, of course, powder diffraction studies may not rule out very subtle additional distortions. In the case of phase S we believe the proposed model is unambiguous and provides a novel and well-characterized example of a *compound* tilt system (i.e., one in which two different tilt *irreps* coexist relative to a single-crystallographic axis) in a perovskite. In the case of the more complex phase R, two structural models are proposed, both of which display unique and complex tilt systems. Discrimination between the two models is difficult, even from this combination of highest resolution NPD/SXPD and DFT calculations: single-crystal XRD would be required to help clarify the correct model further. Nevertheless, we might speculate that the R-P3 in space group *Pmmn* is preferred because (i) the partially constrained models R-P3c/R-P4c invariably produce the better Rietveld fits as a function of temperature (Table S2, Supporting Information), (ii) DFT calculations give a slightly lower energy for the unoptimized R-P3 versus R-P4 models, and, most significantly perhaps, (iii) Sakowski-Cowley deduced essentially the same R-P3 model independently from a very different experiment and using a very different methodology! Although that work could not comprehensively exclude several other space groups based on systematic absences, a well-reasoned approach to deducing the model was used. Of course, we cannot rule out the possibility that both T_4-mode tilts coexist at the nanostructural level, an

dx.doi.org/10.1021/ic3006585 | *Inorg. Chem.* 2012, 51, 6876−6889

option which is not unreasonable given their structural and energetic similarities.

Comparisons to the other previously suggested models for these complex phases show that problems related to lack of resolution in powder diffraction patterns, missed superlattice reflections in single-crystal XRD, and phase coexistence in some samples precluded identification of correct models. We emphasize that an analysis such as this pushes the limitations of current powder diffraction techniques: a combination of the highest resolution together with a systematic symmetry mode analysis is essential in order to avoid some of the pitfalls referred to herein. Some of the preliminary, higher symmetry models we considered en route to our final models would almost certainly fit equally well to powder diffraction data of only slightly inferior resolution.

$NaNbO_3$ represents the most structurally complex 'simple' perovskite (i.e., one of a fixed ABO_3 composition) known. Although larger and more complex supercells have been suggested in mixed cation systems,[37,38] it is probable that these longer range structural modulations are due, in part, to compositional modulations and definitive models would be difficult to verify. Ultimately, the underlying reasons for the highly complex polymorphism behavior in an apparently 'simple' compound such as $NaNbO_3$ remain to be addressed.

■ ASSOCIATED CONTENT

Supporting Information

Further Rietveld refinement plots, crystal structure plots, CIF files, and ISODISTORT mode decomposition details. This material is available free of charge via the Internet at http://pubs.acs.org.

■ AUTHOR INFORMATION

Corresponding Author

*E-mail: pl@st-and.ac.uk.

Notes

The authors declare no competing financial interest.

■ ACKNOWLEDGMENTS

We thank Prof. Chiu Tang, Mr. Lewis Downie, and Dr. Sandra Reisinger for experimental assistance and EPSRC for a DTG studentship to M.D.P. We thank Diamond Light Source (award no. EE6108) and STFC for provision of experimental facilities and EaStCHEM for computational support through the EaStCHEM Research Computing Facility.

■ REFERENCES

(1) Lines, M. E. Glass, A. M. *Principles and applications of ferroelectrics and related materials*; OUP, 1977.
(2) Saito, Y.; Takao, H.; Tani, T.; Nonoyama, T.; Takatori, K.; Homma, T.; Nagaya, T.; Nakamura, M. *Nature* **2004**, *432*, 84.
(3) Lefkowitz, I.; Lukaszewicz, K.; Megaw, H. D. *Acta Crystallogr.* **1966**, *20*, 670.
(4) Sakowski-Cowley, A. C. Ph.D. Thesis, University of Cambridge, 1967.
(5) Megaw, H. D. *Acta Crystallogr.* **1968**, *A24*, 589.
(6) Ahtee, M.; Glazer, A. M.; Megaw, H. D. *Philos. Mag.* **1972**, *26*, 995.
(7) Glazer, A. M.; Megaw, H. D. *Acta Crystallogr.* **1973**, *A29*, 489.
(8) Megaw, H. D. *Ferroelectrics* **1974**, *7*, 87.
(9) Johnston, K. E.; Tang, C. C.; Parker, J. E.; Knight, K. S.; Lightfoot, P.; Ashbrook, S. E. *J. Am. Chem. Soc.* **2010**, *132*, 8732.
(10) Johnston, K. E.; Griffin, J. M.; Walton, R. I.; Dawson, D. M.; Lightfoot, P.; Ashbrook, S. E. *Phys. Chem. Chem. Phys.* **2011**, *13*, 7565.
(11) Shiratori, Y.; Magrez, A.; Dornseiffer, J.; Haegel, F.-H.; Pithan, C.; Waser, R. *J. Phys. Chem. B* **2005**, *109*, 20122.
(12) Modeshia, D. R.; Darton, R. J.; Ashbrook, S. E.; Walton, R. I. *Chem. Commun.* **2009**, 68.
(13) Darlington, C. N. W.; Megaw, H. D. *Acta Crystallogr.* **1973**, *B29*, 2171.
(14) Sakowski-Cowley, A. C.; Lukaszewicz, K.; Megaw, H. D. *Acta Crystallogr.* **1969**, *B25*, 851.
(15) Glazer, A. M.; Megaw, H. D. *Philos. Mag.* **1972**, *25*, 1119.
(16) Darlington, C. N. W.; Knight, K. S. *Acta Crystallogr.* **1999**, *B55*, 24.
(17) Glazer, A. M. *Acta Crystallogr.* **1972**, *B28*, 3384.
(18) Woodward, P. M. *Acta Crystallogr.* **1997**, *B53*, 32.
(19) Darlington, C. N. W.; Knight, K. S. *Physica B* **1999**, *266*, 368.
(20) Yuzyuk, Yu. I.; Simon, P.; Gagarina, E.; Hennet, L.; Thiaudiere, D.; Torgashev, V. I.; Raevskaya, S. I.; Raevskii, I. P.; Reznitchenko, L. A.; Sauvajol, J. L. *J. Phys.: Condens. Matter* **2005**, *17*, 4977.
(21) Koruza, J.; Tellier, J.; Malic, B.; Bobnar, V.; Kosec, M. *J. Appl. Phys.* **2010**, *108*, 113509.
(22) Mishra, S. K.; Mittal, R.; Pomjakushin, V. Yu.; Chaplot, S. L. *Phys. Rev. B* **2011**, *83*, 134105.
(23) Machado, R.; Sepliarsky, M.; Stachiotti, M. G. *Phys. Rev. B* **2011**, *84*, 134107.
(24) Vanderbilt, D.; Zhong, W. *Ferroelectrics* **1998**, *181*, 206.
(25) Howard, C. J.; Stokes, H. T. *Acta Crystallogr.* **1998**, *B54*, 782.
(26) Orobengoa, D.; Capillas, C.; Aroyo, M. I.; Perez-Mato, J. M. *J. Appl. Crystallogr.* **2009**, *42*, 820.
(27) Campbell, B. J.; Stokes, H. T.; Tanner, D. E.; Hatch, D. M. *J. Appl. Crystallogr.* **2006**, *39*, 607.
(28) Thompson, S. P.; Parker, J. E.; Potter, J.; Hill, T. P.; Birt, A.; Cobb, T. M.; Yuan, F.; Tang, C. C. *Rev. Sci. Instrum.* **2009**, *39*, 075107.
(29) Larson, A. C.; von Dreele, R. B. Los Alamos National Laboratory, Report No. La-UR-86-748, 1987.
(30) Clark, S. J.; Segall, M. D.; Pickard, C. J.; Hasnip, P. J.; Probert, M. J.; Refson, K.; Payne, M. C. *Z. Kristall.* **2005**, *220*, 567.
(31) Pickard, C. J.; Mauri, F. *Phys. Rev. B* **2001**, *63*, 245101.
(32) Yates, J. R.; Pickard, C. J.; Mauri, F. *Phys. Rev. B* **2007**, *76*, 024401.
(33) Howard, C. J.; Withers, R. L.; Knight, K. S.; Zhang, Z. *J. Phys. Condens. Matter* **2008**, *20*, 135202.
(34) Carlsson, S. J. E.; Azuma, M.; Shimakawa, Y.; Takano, M.; Hewat, A.; Attfield, J. P. *J. Solid State Chem.* **2008**, *181*, 611.
(35) Woodward, P. M.; Sleight, A. W.; Vogt, T. J. *Phys. Chem. Solids* **1995**, *56*, 1305.
(36) Campbell, B. J.; Evans, J. S. O.; Perselli, F.; Stokes, H. T. *IUCr Computing Commission Newslett.* **2007**, 81−95.
(37) Tripathi, S.; Pandey, D.; Mishra, S. K.; Krishna, P. S. R. *Phys. Rev. B* **2008**, *77*, 052104.
(38) Garcia-Martin, S.; King, G.; Urones-Garrote, E.; Nénert, G.; Woodward, P. M. *Chem. Mater.* **2011**, *23*, 163.